

**A MINIMALISTIC APPROACH FOR FUNCTIONAL
SELF-ASSEMBLING PEPTIDE AND PSEUDOPEPTIDE
SYSTEMS**

SAMEER DHAWAN



**DEPARTMENT OF CHEMISTRY
INDIAN INSTITUTE OF TECHNOLOGY DELHI
JUNE 2021**

© Indian Institute of Technology Delhi (IITD), New Delhi, 2021

**A MINIMALISTIC APPROACH FOR FUNCTIONAL
SELF-ASSEMBLING PEPTIDE AND PSEUDOPEPTIDE
SYSTEMS**

by

SAMEER DHAWAN

Department of Chemistry

Submitted

in fulfillment of the requirements of the degree of Doctor of Philosophy

to the



Indian Institute of Technology Delhi

June 2021

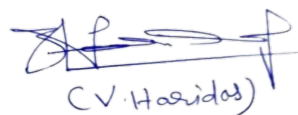
Dedicated in the Lotus Feet of My Revered Master

'H. H. SHRI ASHUTOSH MAHARAJ JI'

Founder & Head of DIVYA JYOTI JAGRATI SANSTHAN (DJJS)...

CERTIFICATE

This is to certify that the thesis entitled, "**A Minimalistic Approach for Functional Self-Assembling Peptide and Pseudopeptide Systems**", being submitted by **Mr. Sameer Dhawan**, to the Indian Institute of Technology Delhi, for the award of degree of **Doctor of Philosophy in Chemistry**, is a record of bonafide research work carried out by him. **Mr. Sameer Dhawan** has worked under my guidance and supervision and has fulfilled all the requirements for the submission of this thesis, which to my knowledge has reached the requisite standard. The results embodied in this thesis have not been submitted in part or in full, to any other University or Institute for award of any degree or diploma.



(V. Haridas)

Dr. V. Haridas

Professor

Department of Chemistry,

Indian Institute of Technology Delhi,

Hauz Khas, New Delhi-110016, India.

ACKNOWLEDGEMENTS

Firstly, I would like to pay my humble salutations in the lotus feet of my revered master “**His Holiness Shri Ashutosh Maharaj Ji**” who inspired me to take up Ph.D. in Chemistry and blessed me with His direct/indirect divine guidance throughout my academic career.

It gives me an immense pleasure to express my deepest gratitude for my research supervisor, **Dr. V. Haridas**, Professor, Department of Chemistry, IIT Delhi, who has been of constant support to me during my Ph.D. period. The scientific discussions with him have considerably improved my approach towards the scientific problems. His critical suggestions have uplifted my level of thinking, working, and writing. His generous supervision made my days enjoyable at IIT Delhi. It was indeed a great opportunity to work under his magnificent guidance.

I extend my thanks to the erstwhile and the present Head of the Department of Chemistry, Prof. Ravi Shankar, Prof. Ashok K. Ganguli and Prof. Anil J. Elias for providing all the facilities essential for my research work. I feel honored to have such a great SRC members Prof. Nalin Pant, Prof. N. G. Ramesh and Prof. Bishwajit Kundu who gave their valuable suggestions to improve the quality of my research work. I am also greatly indebted to my collaborators Prof. Manidipa Banerjee (Kusuma School of Biological Sciences), Prof. Samaresh Das (Centre for Applied Research in Electronics), Prof. Pravin P. Ingole, Prof. Siddharth Pandey, Dr. Harsha Devnani, Sukanya Ghosh, Akshay Moudgil, Vaishali Khokhar and Soniya Gahlawat for their kind help in interdisciplinary experiments. The assistance from Prof. M. Ali Haider (Department of Chemical Engineering), Prof. N. M. Anoop Krishnan (Department of Civil Engineering), Dr. Manish Agarwal, Dr. Tuhin S. Khan, Ravinder is highly acknowledged for DFT calculations and MD simulations. I would also like to acknowledge all the technical staff of Chemistry Department, Mr. J. P. Sharma, Mr. Narugopal, Mr. Keshav, and Mrs. Shubhra for their help in

data acquisition. It is indispensable to thank Mrs. Dimple Hindwani, Mr. Vinod, Mr. Ashish, and Ms. Namita for their frequent guidance in administrative work. The Central Research Facility (CRF) and Nanoscale Research Facility (NRF), IIT Delhi is also acknowledged for providing SEM, HR-TEM, Cryo-TEM, AFM, NMR and Confocal Microscopy facilities.

My special thanks are due to Mr. Gaurav Shankhwar for drawing all the CorelDraw Graphics of the thesis, Mr. Upanshu Gangwar for NMR, Ms. Bharti Singh and Ms. Archishmati Dubey for help in solving the single crystal data. I would also like to thank my lab mates Dr. Jisha Babu, Dr. Appa Rao Sapala, Dr. Bijesh M. B., Dr. Praveen Kumar P. P., Dr. Ishanki Bhardwaj, Dr. Sakshi Sharma, Govind, Rachit, Hanuman, Pushpendra, Akhilesh, Sharan, Anuj, Lakshya, and Sanjay for their support. I wish to thank my postgraduate and undergraduate teachers Dr. Raman K Verma, Late Sh. H.C. Bhalla, Mr. Sameer Sabharwal, Mr. Pankaj Verma, and Mrs. Prabha Deepak who developed my interest in chemistry.

The financial aid from Department of Science & Technology (DST), Government of India in the form of INSPIRE Fellowship is gratefully acknowledged.

I am highly indebted to **Divya Jyoti Jagrati Sansthan (DJJS)**, a socio-spiritual organisation that adopted our family after the sudden demise of my father Late Sh. Surinder Kumar Dhawan and afforded my whole study since 2005. I would like to thank my whole **DJJS family** for their unconditional love and encouragement.

Last but not the least, I express my gratitude towards my Mother Smt. Kanchan Dhawan, Brother Sw. Vigyananand and Sister Sadhvi Monika Bharti for their constant affection and support.

New Delhi

June 2021



Sameer Dhawan

ABSTRACT

The thesis entitled "**A Minimalistic Approach for Functional Self-Assembling Peptide and Pseudopeptide Systems**" presents the modest designs of peptide and pseudopeptide molecules for the multifaceted applications in the diverse fields of nanotechnology and biotechnology. In addition, we have explored a hitherto unknown class of vesicles altogether different from the conventional bilayer vesicles. The work presented in the thesis has been divided into five chapters.

Chapter 1

Chapter 1 gives a panoramic view of designer peptide and pseudopeptide systems in a systematic manner encompassing all the preliminary designs as well as the recent advancements. A variety of self-assembling peptidic systems ranging from short peptides, amphiphilic peptides, cyclic peptides, linear peptides to polymeric peptides have been reviewed thoroughly. The mechanistic insight into the formation of nanotubes and vesicles using different strategies proposed in the literature, is also given. In addition, the diverse applications of designer peptides in the field of drug delivery, anion sensing and organic electronics is highlighted.

Chapter 2

Chapter 2 deals with the design, synthesis and self-assembling properties of a series of cystine-cored minimalistic dipeptides that exhibited the prominent redox-responsive behavior. Various experimental as well as the computational investigations were performed to reveal the self-assembling mechanism of dipeptides in water. Further, the encapsulation of drug molecules by the vesicle-forming dipeptide and their subsequent redox-triggered sustained release in an intracellular milieu is demonstrated.

Chapter 3

Chapter 3 presents the minimalistic design strategy for the development of amino acid appended supersensitive anion sensors that can detect anions in both aqueous as well as organic media. Various spectroscopic and electrochemical measurements were performed to demonstrate the ultratrace sensing of anions in water with the lowest limit of detection values reported so far. Further, the self-assembled morphologies of the host molecules were also investigated using different ultramicroscopic techniques.

Chapter 4

Chapter 4 outlines the fabrication of organic field effect transistors (OFETs) in a bottom-gate/bottom-contact configuration using the self-assembling peptidic polydiacetylenes. The peptide-based OFETs were found to exhibit a p-type FET behavior with an exceptionally high hole mobility of up to $9.29 \text{ cm}^2 \text{ V}^{-1} \text{ s}^{-1}$ at room temperature. The key role of aromatic amino acids in providing high mobility values to the OFET is highlighted.

Chapter 5

Chapter 5 describes the new class of vesicles named as “reverse micellar vesicles”, possessing dual features of classical micelles and conventional vesicles. The novel model of vesicles was established by using a series of self-assembling pseudopeptidic polymers that were synthesized by the ring opening metathesis polymerization (ROMP) of lipidated amino acids appended norbornene monomers. The comprehensive ultramicroscopic and spectroscopic analyses were performed to delineate the hierarchical mechanism of formation of reverse micellar vesicles.

सारांश

थीसिस शीर्षक "उपादेय स्व-संयोजित पेष्टाइड और स्यूडोपेष्टाइड सिस्टम्स के लिए एक सरलतम कार्यनीति" नैनो प्रौद्योगिकी और जैव प्रौद्योगिकी के विविध क्षेत्रों में बहुआयामी अनुप्रयोगों के लिए पेष्टाइड और स्यूडोपेष्टाइड यौगिकों के सरलतम डिजाइन प्रस्तुत करता है। इसके अलावा, हमने पुटिकाओं के एक नवीनतम वर्ग का पता लगाया है जो पारंपरिक बाइलेयर पुटिकाओं से बिल्कुल अलग है। थीसिस में प्रस्तुत कार्य को पाँच अध्यायों में विभाजित किया गया है।

अध्याय 1

अध्याय 1 सभी प्रारंभिक डिजाइनों के साथ-साथ हालिया प्रगति को शामिल करते हुए एक व्यवस्थित तरीके से डिजाइनर पेष्टाइड और स्यूडोपेष्टाइड सिस्टम्स का एक विहंगम दृश्य प्रस्तुत करता है। लघु पेष्टाइड्स, एम्फीफिलिक पेष्टाइड्स, चक्रीय पेष्टाइड्स, रैखिक पेष्टाइड्स से लेकर बहुलक पेष्टाइड्स तक के विभिन्न प्रकार के स्व-संयोजित पेष्टाइडिक प्रणालियों की अच्छी तरह से समीक्षा की गई है। साहित्य द्वारा प्रस्तावित विभिन्न रणनीतियों का उपयोग करके नैनोट्यूब और पुटिकाओं के निर्माण में निहित पद्धतियों की अंतर्विवेचना भी प्रस्तुत की गयी है। इसके अलावा, दवा वितरण, आयन सेंसिंग और ऑर्गेनिक इलेक्ट्रॉनिक्स के क्षेत्र में डिजाइनर पेष्टाइड्स के विविध अनुप्रयोगों पर प्रकाश डाला गया है।

अध्याय 2

अध्याय 2 सिस्टीन-कोर डाइपेष्टाइड्स की सरलतर श्रृंखला के डिजाइन, संश्लेषण और स्व-संयोजन गुणों से संबंधित है, जो प्रमुखतः रेडॉक्स-संवेदनशील व्यवहार का प्रदर्शन करते हैं। पानी में डाइपेष्टाइड्स के स्व-संयोजन तंत्र को प्रकट करने के लिए विभिन्न प्रयोगात्मक और कम्प्यूटेशनल जांच की गई है। इसके

अतिरिक्त, पुटिका बनाने वाले डाइपेण्डेड द्वारा दवा के अणुओं के एनकैप्सुलेशन और इंटरसेल्युलर परिवेश में उनके रेडॉक्स-ट्रिगर निरंतर रिलीज को प्रदर्शित किया गया है।

अध्याय 3

अध्याय 3 अमीनो एसिड्स युक्त सुपरसेंसिटिव आयन सेंसर के विकास के लिए सरलतम डिजाइन पद्धति प्रस्तुत करता है, जो जलीय और कार्बनिक मीडिया दोनों में आयनों का पता लगा सकते हैं। पानी में आयनों की अल्ट्राट्रेस सेंसिंग को प्रदर्शित करने के लिए विभिन्न स्पेक्ट्रोस्कोपिक और इलेक्ट्रोकेमिकल माप किए गए हैं, जो अब तक के साहित्य में वर्णित डिटेक्शन वैल्यू की न्यूनतम सीमा दर्शाते हैं। इसके अलावा, विभिन्न अल्ट्रासाइक्रोस्कोपिक तकनीकों का उपयोग करके मेजबान अणुओं की स्व-संयोजित आकारिकी की भी जांच की गई।

अध्याय 4

अध्याय 4 स्व-संयोजित पेप्टिडिक पॉलीडायसेटिलीनों द्वारा बॉटम-गेट/बॉटम-कॉन्टैक्ट कॉन्फ़िगरेशन में ऑर्गेनिक फील्ड इफेक्ट ट्रांजिस्टर (OFETs) के निर्माण की रूपरेखा प्रदर्शित करता है। पेण्डेड-आधारित OFETs को कमरे के तापमान पर $9.29 \text{ cm}^2 \text{ V}^{-1} \text{ s}^{-1}$ तक की असाधारण उच्च होल मोबिलिटी (Hole Mobility) के साथ p-प्रकार का FET व्यवहार प्रदर्शित करते दर्शाया गया है। OFET को उच्च मोबिलिटी मूल्य प्रदान करने में एरोमेटिक अमीनो एसिड्स की महत्वपूर्ण भूमिका पर प्रकाश डाला गया है।

अध्याय 5

अध्याय 5 पुटिकाओं के नवीनतम वर्ग का वर्णन करता है जिसे "रिवर्स माइसलर वेसिकल्स" नाम दिया गया है, जिसमें क्लासिकल माइसल्स और पारंपरिक पुटिकाओं की दोहरी विशेषताएं हैं। पुटिकाओं का नया मॉडल स्व-संयोजित स्यूडोपेप्टिडिक पॉलीमर्स की एक श्रृंखला का उपयोग करके स्थापित किया गया है, जो

लिपिडेटेड अमीनो एसिड्स युक्त नॉरबोर्निन मोनोमर्स के रिंग ओपनिंग मेटाथिसिस पोलिमराइजेशन (ROMP) द्वारा संश्लेषित होते हैं। रिवर्स माइसलर वेसिकल्स के गठन में निहित पदानुक्रमित तंत्र को चित्रित करने के लिए व्यापक अल्ट्रासाइक्रोस्कोपिक और स्पेक्ट्रोस्कोपिक विश्लेषण किए गए हैं।

TABLE OF CONTENTS

	Page No.
Certificate	i
Acknowledgements	ii
Abstract	iv
Contents	ix
List of Figures	xiv
List of Tables	xxxii
List of Schemes	xxxiii
List of Abbreviations	xxxiv
Notes	xl
CHAPTER 1: Introduction	1
1.1 Molecular Self-Assembly	3
1.2 Self-Assembling Peptides & Pseudopeptides	5
1.3 Peptide and Pseudopeptide Nanostructures	9
1.3.1 Nanotubes	9
1.3.1.1 Cyclic Peptides	10
1.3.1.2 Acyclic Peptides	13
1.3.1.3 Short Peptides	15
1.3.2 Nanofibers	19
1.3.2.1 Acyclic Peptides	19

1.3.2.2 Cyclic Peptides	25
1.3.2.3 Short Peptides	30
1.3.2.4 Polymeric Peptides	34
1.3.3 Vesicles	36
1.3.3.1 Short Peptides	36
1.3.3.2 Cyclic Peptides	40
1.3.3.3 Polymeric Peptides	44
1.4 Mechanism of Self-Assembly	48
1.5 Applications of Self-Assembling Peptides and Pseudopeptides	50
1.5.1 Drug Delivery	51
1.5.2 Anion Binding	57
1.5.3 Organic Electronics	65
1.6 Conclusions	71
1.7 References	72
CHAPTER 2: Redox Sensitive Self-Assembling Dipeptides for Sustained Intracellular Drug Delivery	98
2.1 Introduction	100
2.2 Results and Discussion	102
2.2.1 Design and Synthesis	102
2.2.2 Investigation of Self-Assembly	104
2.2.3 Molecular Dynamics (MD) Simulations	107
2.2.4 Drug Encapsulation	112

2.2.5 <i>In Vitro</i> Drug Release Studies	115
2.2.6 Stability Studies	120
2.3 Conclusions	121
2.4 Experimental Section	122
2.5 References	142
CHAPTER 3: Supersensitive Anion Sensing in Pure Organic and Aqueous Media by Amino Acids Conjugated Ellman's Reagent	151
3.1 Introduction	153
3.2 Results and Discussion	155
3.2.1 Design and Synthesis	155
3.2.2 Anion Sensing in Organic Media	158
3.2.2.1 UV-Vis Spectroscopic Studies	158
3.2.2.2 ¹ H NMR Studies	167
3.2.2.3 Density Functional Theory (DFT) Calculations	173
3.2.3 Anion Sensing in Aqueous Media	179
3.2.3.1 Fabrication of Electrochemical Anion Sensor	179
3.2.3.2 Electrochemical Studies	181
3.2.4 Investigation of Self-Assembly	187
3.3 Conclusions	190
3.4 Experimental Section	191
3.5 References	203

CHAPTER 4: Organic Field Effect Transistors Based on Self-Assembling Core-Modified Peptidic Polymers	214
4.1 Introduction	216
4.2 Results and Discussion	217
4.2.1 Design and Synthesis	217
4.2.2 Cyclic Voltammetry (CV)	224
4.2.3 Device Fabrication & Investigation of Self-Assembly	225
4.2.4 OFET Characterization	227
4.2.5 Stability and Repeatability Studies	231
4.3 Conclusions	232
4.4 Experimental Section	233
4.5 References	245
CHAPTER 5: Unprecedented Formation of “Reverse Micellar Vesicles” from Pseudopeptidic Bottlebrush Polymers	251
5.1 Introduction	253
5.2 Results and Discussion	254
5.2.1 Design and Synthesis	254
5.2.2 Investigation of Self-Assembly	265
5.2.3 Anatomy of Vesicles	270
5.2.4 Mechanism of Formation	274
5.2.5 Substrate Scope	279
5.3 Conclusions	291

5.4 Experimental Section	292
5.5 References	339
Curriculum Vitae	345

LIST OF FIGURES

Figure No.	Description	Page No.
Figure 1.1	Various non-covalent interactions involved in the molecular self-assembly.	4
Figure 1.2	Graphical representation of protein folding showing different levels of protein structure.	5
Figure 1.3	Diverse designer synthetic self-assembling systems.	6
Figure 1.4	Chemical structure of a macrocyclic pseudopeptide A1 .	7
Figure 1.5	Design strategies for the synthesis of pseudopeptides.	8
Figure 1.6	a) Chemical structure of an octapeptidic macrocycle A2 and b) self-assembly of cyclic subunits to form a tubular architecture.	10
Figure 1.7	Molecular structures of cyclic octapeptides A3-A4 , decapeptide A5 and dodecapeptide A6 .	11
Figure 1.8	Chemical structure of naturally-occurring cyclopeptide Lanereotide A7 .	12
Figure 1.9	Chemical structure of peptide-triazole hybrid macrocycle A8 .	13
Figure 1.10	Chemical structure of heptane bolaamphiphile A9 .	14
Figure 1.11	Chemical structures of Phe-containing bolaamphiphiles A10-A13 .	15
Figure 1.12	a) Chemical structure of Phe-Phe dipeptide A14 and b) schematic showing silver nanowire casting within the A14 nanotubes.	16
Figure 1.13	Chemical structures of self-assembling dipeptides A15-A20 .	17
Figure 1.14	Chemical structures of self-assembling tripeptides A21-A22 .	17
Figure 1.15	Chemical structures of stereoisomers A23-A24 of fluorine-substituted dipeptide.	18

Figure 1.16	Chemical structures of acyclic pseudopeptides A25-A26 .	18
Figure 1.17	Chemical structures of RADA16-I peptide A27 and its variants A28-A31 modified with RGD-moieties (highlighted in blue).	20
Figure 1.18	Chemical structures of self-assembling Phe-based peptides A32-A35 .	21
Figure 1.19	Chemical structures of peptide amphiphiles A36-A37 and PAG.	22
Figure 1.20	Chemical structures of serine-based lipopeptides A38-A40 .	23
Figure 1.21	Chemical structure of lipidated Glu-based pseudopeptide A41 and its concentration-induced nanoflower self-assembly.	24
Figure 1.22	Chemical structures of cyclic pseudopeptides A42-A48 .	25
Figure 1.23	Chemical structure of cationic peptide A49 and its guanidinylated derivative A50 .	26
Figure 1.24	Chemical structure of naturally occurring orbitide LOB3 A51 .	26
Figure 1.25	a) Chemical structures of pseudopeptidic macrocycles A54-A55 and b) cartoon diagram showing the self-assembly of A54 into amyloid fibrils.	29
Figure 1.26	Chemical structures of Fmoc-protected dipeptides A56-A64 .	30
Figure 1.27	Chemical structure of PEGylated hexapeptide A65 .	31
Figure 1.28	Chemical structures of DOPA-based dipeptides A66-A67 .	32
Figure 1.29	Chemical structures of Amoc-protected Phe-Phe dipeptide A68 , Phe- Δ Phe dipeptide A69 and Fmoc-protected Phe-Phe-Phe tripeptide A70 .	32
Figure 1.30	a) Chemical structures of Phe-Phe-based tripeptides A71-A72 and b) cartoon representation of ultrasound-induced morphological transition.	33
Figure 1.31	Chemical structures Phe-Phe dipeptide A14 , Phg-Phg dipeptide A73 , Cys-Phe-Phe tripeptide A74 and their respective morphologies in aqueous dispersions.	36

Figure 1.32	Chemical structures of aliphatic dipeptides A80-A82 .	38
Figure 1.33	Molecular structures of tryptophan-based tripodal dipeptides A83-A84 .	39
Figure 1.34	Chemical structures of Trp-containing tripodal pseudopeptides A85-A87 .	40
Figure 1.35	Chemical structures of Arg-Trp based cyclic and linear peptides A88-A89 .	41
Figure 1.36	Chemical structures of amphipathic peptide-triazole hybrid macrocycles A90-A92 .	41
Figure 1.37	Chemical structures of peptide macrocycles A93-A100 .	42
Figure 1.38	Chemical structures of pseudopeptidic macrocycles A101-A102 .	43
Figure 1.39	Chemical structures of amphiphilic diblock copolypeptides A103-A104 .	44
Figure 1.40	Chemical structures of pseudo-polypeptides A105-A107 .	45
Figure 1.41	Schematic illustration showing the pH-induced morphology metamorphosis of A106 .	46
Figure 1.42	Chemical structures of silylated polypeptides A108-A110 .	46
Figure 1.43	Chemical structures of amphiphilic diblock polypeptoids A111-A112 .	47
Figure 1.44	a) Proposed strategies for the formation of nanotubes from the self-assembly of (i) cyclic molecules, (ii) wedge-shaped molecules, (iii) rod-like molecules and (iv) helical molecules; (b) poloidal folding of self-assembled 2D sheet to give tubular architectures.	49
Figure 1.45	Schematic illustration showing the hierarchical formation of vesicles.	49
Figure 1.46	An illustration of diverse supramolecular structures shown by functional self-assembling peptides/pseudopeptides and their applications.	50
Figure 1.47	Chemical structures of cationic Phe-Phe dipeptide A113 and Trp-Phe dipeptide A114 .	51

Figure 1.48	Graphical representation showing the morphological transition of A113 for intracellular oligonucleotide delivery.	52
Figure 1.49	Chemical structures of Lys-Lys dipeptide-5-Fu conjugates A115-A116 .	53
Figure 1.50	Chemical structure of peptide amphiphile A117 .	54
Figure 1.51	Chemical structure of peptide bolaamphiphile-paclitaxel conjugate A120 .	55
Figure 1.52	Chemical structure of synthetic ion-binding cyclic peptide A121 .	58
Figure 1.53	Chemical structure of peptide macrocycle A122 .	59
Figure 1.54	Chemical structures of pseudo-hexapeptide macrocycles A123-A124 .	59
Figure 1.55	Chemical structures of cyclic pseudo-hexapeptides A125-A126 .	60
Figure 1.56	Chemical structures of hybrid biscyclopeptides A127-A130 .	61
Figure 1.57	Chemical structure of fluorescent pseudopeptide A131 .	62
Figure 1.58	Chemical structures of metal-ion-based peptide anion receptors A132-A137 .	63
Figure 1.59	Chemical structures of ferrocene-conjugated RAFTs A138-A139 .	64
Figure 1.60	Chemical structure of thiolated pseudopeptidic macrocycle A140 .	64
Figure 1.61	Schematic representation of the azurin-based FET fabricated in a bottom-gate/top-contact configuration.	65
Figure 1.62	a) Chemical structure of NDI-modified cyclic peptide A141 , b) Reversible reduction of NDI moieties to anion radicals and c) Graphical illustration showing the redox-triggered self-assembly of peptide nanotubes.	66
Figure 1.63	Chemical structure of anthracene-protected tetrapeptide A144 and thiophene-containing lipidated tetrapeptide A145 .	68

Figure 1.64	Chemical structures of TTF-peptide conjugates A146-A147 .	69
Figure 1.65	Chemical structures of heptapeptides A148-A150 .	70
Figure 2.1	Design strategy of self-assembling dipeptide for drug delivery applications.	102
Figure 2.2	Chemical structures of cystine-cored dipeptides based on amino acids Trp, Phe and Leu, respectively a) <i>N</i> -termini Boc-protected B1-B3 , and b) <i>N</i> -deprotected peptides B4-B6 .	103
Figure 2.3	Microscopic and size distribution analyses of B1 . Compound B1 in MeOH (1 mg/mL) a) SEM, b) AFM, c) AFM cross-sectional analysis along the line, d) TEM, e) fluorescence microscopic images of B1 +0.02 equivalents of Rhodamine B ($\lambda_{\text{ex}} = 510\text{-}560$ nm), and f) DLS.	105
Figure 2.4	SEM images of a-b) B2 in MeOH (1 mg/mL) and c-d) B3 in MeOH (1 mg/mL).	105
Figure 2.5	Morphological analysis of B4 dissolved in water (1 mg/mL) a) SEM b) AFM c) AFM cross-sectional analysis along the line d) TEM; e) DLS and f) Scattered intensities collected from the different concentration solutions of B4 in water. The intersection point in the plot corresponds to CAC.	106
Figure 2.6	SEM images of B5 dissolved in water (1 mg/mL).	107
Figure 2.7	a) An initial labeled structure of B4 , b) A snapshot of initial system configuration of flat dipeptide membrane, c) Snapshots of dipeptide membrane (blue) with a spherical fit (red).	108
Figure 2.8	MD simulations of dipeptide B4 a) Progressive folding of B4 flat membrane toward vesicular structures, b) Schematic rendering of vesicle formation, c) Curvature of membrane, $\kappa(\text{\AA}^{-1})$ with respect to time $t(\text{ns})$, d) Pair distribution function $g(r)$ with respect to distance (\AA) for Trp-Trp interactions, e) Snapshot of the arrangement of two dipeptide molecule exhibiting preferential attraction of the indole groups, and f) Pair distribution function $g(r)$ with respect to distance (\AA) for B4 -water interactions.	109
Figure 2.9	Different snapshots showing the arrangement of two B4 molecules	110

exhibiting preferential attraction of the tryptophan groups.

- Figure 2.10 Snapshots of different orientations of **B4** molecule in water showing the preferential attraction of water cloud (gradient shown from white to red) toward backbone than tryptophan residues. A cavity of water can be seen clearly around tryptophan. 111
- Figure 2.11 Encapsulation of drug by vesicles a) Histogram showing the DOX fluorescence intensity distribution at 590 nm, Data shown are the mean± standard deviation (SD) (n = 3), inset shows the chemical structure of DOX, b) DLS showing the increase in diameter of vesicles upon drug entrapment; Microscopic images of swollen vesicles after DOX encapsulation c) SEM, d) TEM, and e) fluorescence microscopic images ($\lambda_{\text{ex}} = 510\text{-}560$ nm). 112
- Figure 2.12 ESI-MS spectra of **B4** a) before and b) after the addition of GSH. 113
- Figure 2.13 Morphological analysis of **B4** vesicles after the addition of GSH (10 mM) a) SEM, b) TEM, and c) AFM. 114
- Figure 2.14 Redox-responsive nature of vesicles a) Release profile of DOX loaded **B4** vesicles at different GSH concentrations and pH values; Cell-viability MTT assay b) cytocompatibility of blank **B4** vesicles on MDA-MB-231 and HeLa cells; Cytotoxicity profile of DOX loaded vesicles on c) MDA-MB-231, and d) HeLa cells. Data represented are mean of independent triplicate results ± SD. *** $p < 0.001$; ** $p < 0.01$; * $p < 0.05$. Student's *t*-test for % viability of DOX loaded **B4** vesicles was performed in comparison to % viability of free DOX base. 116
- Figure 2.15 Optical microscopic images of treated cells after 72 h. 117
- Figure 2.16 CLSM images showing the cellular internalization of DOX loaded vesicles in A) MDA-MB-231, B) HeLa cell lines where a) cells only, b) **B4** treated cells, c) DOX+**B4** treated cells, and d) free DOX treated cells. All the images were captured at 60× magnification. 118
- Figure 2.17 Immunoblotting assay showing an induction of apoptosis mediated cytotoxicity by DOX loaded **B4** vesicles in MDA-MB-231 cells. Cells were treated with empty **B4** vesicles, DOX loaded **B4** vesicles and free DOX for the indicated time periods. Whole cell extracts were prepared 119

and analyzed by immunoblotting using antibodies specific to caspase-3, PARP1 and GAPDH respectively.

Figure 2.18	<i>In vitro</i> stability study of DOX-loaded B4 vesicles stored in the dark at 4 °C.	120
Figure 2.19	Aggregation study of vesicles stored in the dark at 4 °C using DLS-based analysis a) empty B4 vesicles and b) DOX loaded B4 vesicles.	121
Figure 2.20	¹ H NMR (300 MHz, CDCl ₃) spectrum of B1 . (Inset: zoomed aromatic region)	133
Figure 2.21	¹³ C NMR (75 MHz, CDCl ₃) spectrum of B1 .	133
Figure 2.22	ESI-Mass spectrum of B1 .	134
Figure 2.23	¹ H NMR (300 MHz, CDCl ₃) spectrum of B2 . (Inset: zoomed aromatic region)	134
Figure 2.24	¹³ C NMR (75 MHz, CDCl ₃) spectrum of B2 .	135
Figure 2.25	ESI-Mass spectrum of B2 .	135
Figure 2.26	¹ H NMR (300 MHz, CDCl ₃) spectrum of B3 .	136
Figure 2.27	¹³ C NMR (100 MHz, CDCl ₃) spectrum of B3 .	136
Figure 2.28	ESI-Mass spectrum of B3 .	137
Figure 2.29	¹ H NMR (300 MHz, D ₂ O) spectrum of B4 . (Inset: zoomed aromatic region)	137
Figure 2.30	¹³ C NMR (75 MHz, D ₂ O) spectrum of B4 .	138
Figure 2.31	ESI-Mass spectrum of B4 .	138
Figure 2.32	¹ H NMR (300 MHz, CD ₃ OD) spectrum of B5 .	139
Figure 2.33	¹³ C NMR (75 MHz, CD ₃ OD) spectrum of B5 .	139

Figure 2.34	ESI-Mass spectrum of B5 .	140
Figure 2.35	^1H NMR (300 MHz, CD_3OD) spectrum of B6 .	140
Figure 2.36	^{13}C NMR (75 MHz, CD_3OD) spectrum of B6 .	141
Figure 2.37	ESI-Mass spectrum of B6 .	141
Figure 3.1	Design strategy of Ellman's reagent-based anion sensors for the detection of anions in both aqueous and organic media.	155
Figure 3.2	Chemical structures of receptors C1-C3 based on Ellman's reagent.	156
Figure 3.3	An initial screening of anion binding potential of C1 upon addition of 50 equiv. of various anions.	158
Figure 3.4	An initial screening of anion binding potential of C2 upon addition of 50 equiv. of various anions.	159
Figure 3.5	An initial screening of anion binding potential of C3 upon addition of 50 equiv. of various anions.	159
Figure 3.6	UV-vis titration of a) C1 against F^- , b) C2 against F^- , c) C3 against F^- , d) C1 against H_2PO_4^- , e) C2 against H_2PO_4^- , and f) C3 against H_2PO_4^- .	160
Figure 3.7	Colorimetric response of sensors in acetonitrile upon addition of 3.0 equiv. of different anions a) C1 , b) C2 and c) C3 .	161
Figure 3.8	Determination of LOD of chemosensors with anions. a) C1 with F^- , b) C1 with H_2PO_4^- , c) C2 with F^- , d) C2 with H_2PO_4^- , e) C3 with F^- , and f) C3 with H_2PO_4^- .	162
Figure 3.9	Job plots of host with anions a) C1 with F^- , b) C2 with F^- , c) C3 with F^- , d) C1 with H_2PO_4^- , e) C2 with H_2PO_4^- , and f) C3 with H_2PO_4^- .	163
Figure 3.10	Fitting and residual plots for UV-vis titrations as obtained from BindFit a) C1 with F^- , b) C1 with H_2PO_4^- , c) C2 with F^- , d) C2 with H_2PO_4^- , e) C3 with F^- , and f) C3 with H_2PO_4^- . BindFit URLs are given for respective titration.	166
Figure 3.11	Stack plots of ^1H NMR spectra (500 MHz, $\text{CD}_3\text{CN}:\text{DMSO}-d_6$ 9:1) of C1 with increasing amount of TBAF. The region of protons involved in the	168

binding is shown.

Figure 3.12	Stack plots of ^1H NMR spectra (500 MHz, $\text{CD}_3\text{CN}:\text{DMSO-}d_6$ 9:1) of C1 with increasing amount of TBAH_2PO_4 . The region of protons involved in the binding is shown.	168
Figure 3.13	Stack plots of ^1H NMR spectra (500 MHz, $\text{CD}_3\text{CN}:\text{DMSO-}d_6$ 9:1) of C2 with increasing amount of TBAF. The region of protons involved in the binding is shown.	169
Figure 3.14	Stack plots of ^1H NMR spectra (500 MHz, $\text{CD}_3\text{CN}:\text{DMSO-}d_6$ 9:1) of C2 with increasing amount of TBAH_2PO_4 . The region of protons involved in the binding is shown.	169
Figure 3.15	Stack plots of ^1H NMR spectra (500 MHz, $\text{CD}_3\text{CN}:\text{DMSO-}d_6$ 9:1) of C3 with increasing amount of TBAF. The region of protons involved in the binding is shown.	170
Figure 3.16	Stack plots of ^1H NMR spectra (500 MHz, $\text{CD}_3\text{CN}:\text{DMSO-}d_6$ 9:1) of C3 with increasing amount of TBAH_2PO_4 . The region of protons involved in the binding is shown.	171
Figure 3.17	Variation in the ^1H NMR chemical shifts (δ ppm) of the alpha $-\text{CH}$ as a function of equivalents of anions added.	172
Figure 3.18	Optimized geometries of (a-c) C1 , (d-f) C2 and (g-i) C3 , in folded- and extended- conformations. Relative energy (E_{rel}) of the structure is mentioned in kJ/mol. Color code: Sulfur (yellow), Nitrogen (blue), Carbon (silver), Oxygen (red), Hydrogen (white).	174
Figure 3.19	Optimized geometries of host-guest complex of F^- ion with a) C1 , b) C2 and c) C3 . Color code: Sulfur (yellow), Nitrogen (blue), Carbon (silver), Oxygen (red), Hydrogen (white), Fluorine (green). Hydrogen atoms involved in the H-bonding with F^- ion are presented in sky-blue color.	175
Figure 3.20	Structure pool of DFT optimized geometries of C1 + F^- complexes. Color code: Sulfur (yellow), Nitrogen (blue), Carbon (silver), Oxygen (red), Hydrogen (white), Fluorine (green). Hydrogen atoms involved in the H-bonding with F^- ion are presented in sky-blue color.	176
Figure 3.21	Structure pool of DFT optimized geometries of C1 + H_2PO_4^- complex. Color code: Sulfur (yellow), Nitrogen (blue), Carbon (silver), Oxygen (red), Hydrogen (white), Phosphorus (purple). Hydrogen atoms involved in the H-bonding with H_2PO_4^- anion are presented in sky-blue	176

color.

Figure 3.22	Optimized geometries of host-guest complex of H_2PO_4^- anion with a) C1 , b) C2 and c) C3 . Color code: Sulfur (yellow), Nitrogen (blue), Carbon (silver), Oxygen (red), Hydrogen (white), Phosphorus (purple). Hydrogen atoms involved in the H-bonding with H_2PO_4^- anion are presented in sky-blue color.	178
Figure 3.23	Schematic representation of the various steps involved in the fabrication of electrochemical sensor.	179
Figure 3.24	CVs obtained for the gold electrodes modified with a) C1 , b) C2 and c) C3 in the absence and presence of 1 ppm of F^- and H_2PO_4^- ions. Scan rate: 100 mV/s, Supporting Electrolyte: 0.1 M NaNO_3 .	180
Figure 3.25	Representative differential pulse voltammograms (DPVs) obtained for the gold electrodes modified with host molecules at different concentration of target anions a) C1 with F^- , b) C1 with H_2PO_4^- , c) C2 with F^- , d) C2 with H_2PO_4^- , e) C3 with F^- , and f) C3 with H_2PO_4^- .	183
Figure 3.26	Plots of difference in redox current intensities with respect to anion concentration a) C1 with F^- , b) C1 with H_2PO_4^- , c) C2 with F^- , d) C2 with H_2PO_4^- (peak current values were taken as marked in Figure 3.25c-d) e) C3 with F^- , and f) C3 with H_2PO_4^- , with a linear fit.	184
Figure 3.27	SEM images in 1:1 methanol:chloroform a) C1 (1 mM) b) C2 (1 mM) c) C3 (1 mM); TEM images of d) C1 (1 mM) e) C2 (1 mM) and f) C3 (1 mM); Histogram showing the size distribution of vesicles g) C2 and h) C3 .	188
Figure 3.28	SEM images in 1:1 methanol:chloroform upon addition of 1 equiv. of anions a) C2 + F^- , b) C2 + H_2PO_4^- , c) C3 + F^- , and d) C3 + H_2PO_4^- . (Inset shows the magnified image).	189
Figure 3.29	^1H NMR (300 MHz, CDCl_3) spectrum of C1 .	198
Figure 3.30	^{13}C NMR (75 MHz, CDCl_3) spectrum of C1 .	198
Figure 3.31	ESI-Mass spectrum of C1 .	199
Figure 3.32	^1H NMR (300 MHz, CDCl_3) spectrum of C2 .	199

Figure 3.33	^{13}C NMR (75 MHz, CDCl_3) spectrum of C2 .	200
Figure 3.34	ESI-Mass spectrum of C2 .	200
Figure 3.35	^1H NMR spectrum (300 MHz, $\text{DMSO-}d_6$) of C3 .	201
Figure 3.36	^{13}C NMR spectrum (75 MHz, $\text{DMSO-}d_6$) of C3 .	201
Figure 3.37	ESI-Mass spectrum of C3 .	202
Figure 4.1	a) Chemical structures of the Phe-based diacetylene-cored peptides D3-D4 , b) The pre-organization requirements for the topochemical polymerization of diacetylenes, c) Chemical structures of Phe-based PDAs PD3 and PD4 .	218
Figure 4.2	FTIR (KBr) spectrum of D3 showing the amide I and amide II regions. (FTIR spectrum of D4 was not recorded due to its immediate polymerization)	220
Figure 4.3	Concentration-dependent ^1H NMR (300 MHz, CDCl_3) of D3 . (Concentration-dependent ^1H NMR spectra of D4 was not recorded due to its immediate polymerization)	221
Figure 4.4	Normalized Raman spectra of diacetylenes and corresponding polydiacetylenes. (Raman spectrum of D4 was not recorded due to its immediate polymerization)	222
Figure 4.5	UV-vis absorption spectra of diacetylene monomers and corresponding polymers. (UV-vis absorption spectrum of D4 was not recorded due to its immediate polymerization)	223
Figure 4.6	a) Cyclic voltammograms of PD3 and PD4 on a glassy carbon in $\text{TBABF}_4/\text{CH}_3\text{CN}$ solution (Scan rate 100 mV/s); Inset shows the zoomed reductive peaks. b) Energy band diagram of PD4 .	224
Figure 4.7	Powder X-ray diffraction pattern of polymer PD4 . (PXRD data of PD3 was not recorded due to its sticky nature)	225
Figure 4.8	a) Schematic representation of the OFET fabricated in a bottom-gate/bottom-contact configuration, b) AFM image showing the PD4 nanofibers with cross-sectional analysis along the line, c) SEM image of the OFET (scale bar – 200 μm); the inset in the blue broken line box shows the 1 μm channel (scale bar – 2 μm), and d) full coverage of PD4	226

nanofibers in the 1 μm channel (scale bar – 500 nm)

Figure 4.9	FET measurements on PD4 a) Output characteristics, b) Transfer characteristics, c) Temperature dependent output characteristics, d) Arrhenius plot with linear fitting for different V_{DS} values, e) Slope extracted from the Arrhenius plot as shown in (d) as a function of V_{DS} ; a y-intercept of 22.6 obtained from linear fit, and f) Drift velocity (v_d) with electric field at lower temperatures (Inset: at room temperature). The OFETs were fabricated with a channel length of 1 μm and a width of 20 μm .	228
Figure 4.10	FET measurements on polymer PD3 a) Output characteristics and b) Transfer characteristics.	229
Figure 4.11	FET performance parameters of polymer PD4 a) Variation of mobility with V_{GS} at room temperature under ambient conditions, b) Distribution of mobility with different temperatures at $V_{\text{DS}} = -3$ V and c) Activation energy estimation.	230
Figure 4.12	Mobility and subthreshold slope (SS) repeatability characteristics of PD4 -based OFET stored under ambient conditions for 30 days.	232
Figure 4.13	^1H NMR (300 MHz, CDCl_3) spectrum of D1 .	240
Figure 4.14	^{13}C NMR (75 MHz, CDCl_3) spectrum of D1 .	240
Figure 4.15	ESI-Mass spectrum of D1 .	241
Figure 4.16	^1H NMR (300 MHz, CDCl_3) spectrum of D2 .	241
Figure 4.17	^{13}C NMR (75 MHz, CDCl_3) spectrum of D2 .	242
Figure 4.18	ESI-Mass spectrum of D2 .	242
Figure 4.19	^1H NMR (500 MHz, $\text{DMSO}-d_6$) spectrum of D3 .	243
Figure 4.20	^{13}C NMR (125 MHz, $\text{DMSO}-d_6$) spectrum of D3 .	243
Figure 4.21	ESI-Mass spectrum of D3 .	244
Figure 5.1	Graphical representation of different types of spherical assemblies a) classical bilayer vesicle b) reverse vesicle c) Janus vesicle d)	253

proposed model 1 and e) proposed model 2; Blue and yellow parts represent hydrophilic and hydrophobic groups, respectively.

Figure 5.2	Chemical structures of polymers PE5-PE10 along with the graphical representation of corresponding bottlebrush polymeric architecture.	257
Figure 5.3	¹ H NMR (300 MHz, CDCl ₃) spectral comparison of a) monomer E5 and b) polymer PE5 .	258
Figure 5.4	GPC profiles of PE5 a) complete chromatogram, and b) expanded region of polymer peak.	259
Figure 5.5	GPC profiles of PE6 a) complete chromatogram, and b) expanded region of polymer peak.	260
Figure 5.6	GPC profiles of PE7 a) complete chromatogram, and b) expanded region of polymer peak.	261
Figure 5.7	GPC profiles of PE8 a) complete chromatogram, and b) expanded region of polymer peak.	262
Figure 5.8	GPC profiles of PE9 a) complete chromatogram, and b) expanded region of polymer peak.	263
Figure 5.9	GPC profiles of PE10 a) complete chromatogram, and b) expanded region of polymer peak.	264
Figure 5.10	Microscopic analysis of PE5 (2 mg/mL) in 1:1 chloroform:methanol a) SEM, b-c) cryo-TEM, d) TEM, e) AFM, and f) height profile analysis of AFM along the line.	266
Figure 5.11	Microscopic analysis of polymer PE6 (2 mg/mL) in 1:1 chloroform:methanol a) SEM, b) TEM, c) AFM, and d) height profile analysis of AFM along the line.	267
Figure 5.12	Microscopic analysis of polymer PE7 (2 mg/mL) in 2:1 chloroform:methanol a) SEM, b) TEM, c) AFM, and d) height profile analysis of AFM along the line.	267
Figure 5.13	Microscopic analysis of polymer PE8 (2 mg/mL) in 1:1 chloroform:methanol a) SEM, b) TEM, c) AFM, and d) height profile analysis of AFM along the line.	268

Figure 5.14	Microscopic analysis of polymer PE9 (2 mg/mL) in 1:1 chloroform:methanol a) SEM, b) TEM, c) AFM, d) and height profile analysis of AFM along the line.	268
Figure 5.15	Microscopic analysis of polymer PE10 (1 mg/mL) in 1:2 chloroform:methanol a) SEM, b) AFM, and d) height profile analysis of AFM along the line.	269
Figure 5.16	Dynamic light scattering (DLS) profiles of polymers (2 mg/mL) in chloroform:methanol a) PE5 , b) PE6 , c) PE7 , d) PE8 and e) PE9 .	269
Figure 5.17	SEM images of monomers (2 mg/mL) a) E5 in 1:1 chloroform:methanol, b) E6 in 1:1 chloroform:methanol, c) E7 in 2:1 chloroform:methanol. The SEM of E8-E10 was not recorded due to their sticky nature.	270
Figure 5.18	Investigation of interior of vesicles a) Confocal microscopic image (60×) of PE5 + 0.1 equiv. of RB (red filter); Fluorescence emission spectra of b) RB loaded PE5 vesicles [RB concentration = 1 μM, slit width = 1 nm], c) Nile red [NR concentration = 5 μM, slit width = 1 nm] and d) pyrene (Py concentration = 5 μM, slit width = 1 nm, ratio of the intensities of band 1-to-band 3 (I_1/I_3) = 1.12 ± 0.05 and 1.08 ± 0.05 for Py and PE5 +Py, respectively] in 1:1 methanol:chloroform under ambient conditions.	272
Figure 5.19	WCA measurement on a) bare glass surface; Glass surface coated with b) PE5 , c) PE6 , d) PE7 , e) PE8 , and f) PE9 .	273
Figure 5.20	Graphical representation of a) bottlebrush polymeric architecture, b) proposed vesicle model, c) classical bilayer model; Illustration of WCA on the glass surface coated with g) proposed vesicle model, and h) classical bilayer vesicles.	274
Figure 5.21	Hierarchical formation of vesicles a-c) Concentration-dependent SEM, TEM and AFM analysis of PE5 revealing the different intermediate stages during vesicle formation (i) 0.0625 mg/mL, (ii) 0.125 mg/mL, (iii) 0.25 mg/mL, (iv) 0.5 mg/mL, and (v) 2 mg/mL (Insets show the zoomed images; Relevant parts are marked by arrows), d) Schematic representation showing the evolution of reverse micellar vesicles.	275
Figure 5.22	SEM images of PE5 (2 mg/mL) in varying composition of methanol and chloroform.	276

Figure 5.23	Partial ATR-FTIR spectra of PE5 in different solvent compositions, showing amide A region.	277
Figure 5.24	SEM images of (a-b) PE7 (2 mg/mL) in 1:1 chloroform:methanol, c) PE10 (2 mg/mL) in 1:1 chloroform:methanol, d) PE10 (1 mg/mL) in 1:1 chloroform:methanol.	278
Figure 5.25	GPC profiles of PE13 a) complete chromatogram, b) expanded region of polymer peak and c) molecular weight distribution of the polymer.	281
Figure 5.26	GPC profiles of PE14 a) complete chromatogram, b) expanded region of polymer peak and c) molecular weight distribution of the polymer.	282
Figure 5.27	GPC profiles of PE15 a) complete chromatogram, b) expanded region of polymer peak and c) molecular weight distribution of the polymer.	283
Figure 5.28	Microscopic analysis (SEM, TEM and AFM) of polymers (2 mg/mL) in 1:1 chloroform:methanol (a-c) PE13 , (d-f) PE14 , (g-i) PE15 .	284
Figure 5.29	SEM images of monomers (2 mg/mL) in 1:1 chloroform:methanol a) E13 , and (b) E14 . The SEM of E15 was not recorded due to its sticky nature.	285
Figure 5.30	X-ray crystal structure of E13 .	286
Figure 5.31	Proposed models showing the rationale behind the low reactivity of <i>endo</i> -isomers of norbornene towards ROMP (a-b) steric factors (c-d) catalyst inhibition.	290
Figure 5.32	¹ H NMR (300 MHz, CDCl ₃) spectrum of E1 .	310
Figure 5.33	¹³ C NMR (75 MHz, CDCl ₃) spectrum of E1 .	310
Figure 5.34	ESI-Mass spectrum of E1 .	311
Figure 5.35	¹ H NMR (300 MHz, CDCl ₃) spectrum of E2 .	311
Figure 5.36	¹³ C NMR (75 MHz, CDCl ₃) spectrum of E2 .	312
Figure 5.37	ESI-Mass spectrum of E2 .	312

Figure 5.38	^1H NMR (300 MHz, CDCl_3) spectrum of E3 .	313
Figure 5.39	^{13}C NMR (75 MHz, CDCl_3) spectrum of E3 .	313
Figure 5.40	ESI-Mass spectrum of E3 .	314
Figure 5.41	^1H NMR (300 MHz, CDCl_3) spectrum of E4 .	314
Figure 5.42	^{13}C NMR (75 MHz, CDCl_3) spectrum of E4 .	315
Figure 5.43	ESI-Mass spectrum of E4 .	315
Figure 5.44	^1H NMR (300 MHz, CDCl_3) spectrum of E5 .	316
Figure 5.45	^{13}C NMR (75 MHz, CDCl_3) spectrum of E5 .	316
Figure 5.46	ESI-Mass spectrum of E5 .	317
Figure 5.47	^1H NMR (300 MHz, CDCl_3) spectrum of E6 .	317
Figure 5.48	^{13}C NMR (75 MHz, CDCl_3) spectrum of E6 .	318
Figure 5.49	ESI-Mass spectrum of E6 .	318
Figure 5.50	^1H NMR (300 MHz, CDCl_3) spectrum of E7 .	319
Figure 5.51	^{13}C NMR (75 MHz, CDCl_3) spectrum of E7 .	319
Figure 5.52	ESI-Mass spectrum of E7 .	320
Figure 5.53	^1H NMR (300 MHz, CDCl_3) spectrum of E8 .	320
Figure 5.54	^{13}C NMR (75 MHz, CDCl_3) spectrum of E8 .	321
Figure 5.55	ESI-Mass spectrum of E8 .	321
Figure 5.56	^1H NMR (300 MHz, CDCl_3) spectrum of E9 .	322

Figure 5.57	^{13}C NMR (75 MHz, CDCl_3) spectrum of E9 .	322
Figure 5.58	ESI-Mass spectrum of E9 .	323
Figure 5.59	^1H NMR (300 MHz, CDCl_3) spectrum of E10 .	323
Figure 5.60	^{13}C NMR (75 MHz, CDCl_3) spectrum of E10 .	324
Figure 5.61	ESI-Mass spectrum of E10 .	324
Figure 5.62	^1H NMR (300 MHz, CDCl_3) spectrum of E11 .	325
Figure 5.63	^{13}C NMR (75 MHz, CDCl_3) spectrum of E11 .	325
Figure 5.64	ESI-Mass spectrum of E11 .	326
Figure 5.65	^1H NMR (300 MHz, CDCl_3) spectrum of E12 .	326
Figure 5.66	^{13}C NMR (75 MHz, CDCl_3) spectrum of E12 .	327
Figure 5.67	ESI-Mass spectrum of E12 .	327
Figure 5.68	^1H NMR (300 MHz, CDCl_3) spectrum of E13 .	328
Figure 5.69	^{13}C NMR (75 MHz, CDCl_3) spectrum of E13 .	328
Figure 5.70	ESI-Mass spectrum of E13 .	329
Figure 5.71	^1H NMR (300 MHz, CDCl_3) spectrum of E14 .	329
Figure 5.72	^{13}C NMR (75 MHz, CDCl_3) spectrum of E14 .	330
Figure 5.73	ESI-Mass spectrum of E14 .	330
Figure 5.74	^1H NMR (300 MHz, CDCl_3) spectrum of E15 .	331
Figure 5.75	^{13}C NMR (75 MHz, CDCl_3) spectrum of E15 .	331

Figure 5.76	ESI-Mass spectrum of E15 .	332
Figure 5.77	^1H NMR (300 MHz, CDCl_3) spectrum of E16 .	332
Figure 5.78	^{13}C NMR (75 MHz, CDCl_3) spectrum of E16 .	333
Figure 5.79	ESI-Mass spectrum of E16 .	333
Figure 5.80	^1H NMR (300 MHz, CDCl_3) spectrum of PE5 .	334
Figure 5.81	^1H NMR (300 MHz, CDCl_3) spectrum of PE6 .	334
Figure 5.82	^1H NMR (300 MHz, CDCl_3) spectrum of PE7 .	335
Figure 5.83	^1H NMR (300 MHz, CDCl_3) spectrum of PE8 .	335
Figure 5.84	^1H NMR (300 MHz, CDCl_3) spectrum of PE9 .	336
Figure 5.85	^1H NMR (300 MHz, CDCl_3) spectrum of PE10 .	336
Figure 5.86	^1H NMR (300 MHz, CDCl_3) spectrum of PE13 .	337
Figure 5.87	^1H NMR (300 MHz, CDCl_3) spectrum of PE14 .	337
Figure 5.88	^1H NMR (300 MHz, CDCl_3) spectrum of PE15 .	338

LIST OF TABLES

Table No.	Description	Page No.
Table 1.1	Summary of designer self-assembling peptides for drug delivery applications.	56
Table 3.1	Binding constant values (M^{-1}) of different hosts as calculated from BindFit software.	167
Table 3.2	Mulliken charges on different H atoms of host molecules as derived from the most stable host-guest geometry.	177
Table 3.3	Oxidation and reduction peak potentials (E) and current values (I) of the gold electrodes modified with host molecules.	181
Table 3.4	Oxidation peak potential values of modified gold electrodes in the absence (E_{free}°) and presence of target anions (E_{bound}°). Measuring conditions are mentioned in Figure 3.24 caption.	182
Table 3.5	Reduction peak potential values of modified gold electrodes in the absence (E_{free}°) and presence of target anions (E_{bound}°). Measuring conditions are mentioned in Figure 3.24 caption.	182
Table 3.6	LOD and LOQ values for the electrochemical sensors.	185
Table 3.7	Comparison of the performance of as-prepared anion sensors with those reported in the literature.	186
Table 4.1	Details of the band structure parameters of polymers.	224
Table 5.1	Molecular weight distribution of polymers as obtained from GPC using THF as eluent.	265
Table 5.2	Crystal data and structure refinement for E13 .	286
Table 5.3	Atomic coordinates ($\times 10^4$) and equivalent isotropic displacement parameters ($\text{\AA}^2 \times 10^3$) for E13 . $U(eq)$ is defined as one third of the trace of the orthogonalized U^{ij} tensor.	288

LIST OF SCHEMES

Scheme No.	Description	Page No.
Scheme 1.1	Synthesis of a dynamic combinatorial library of pseudopeptidic macrocycles by oxidation of acyclic peptide dithiol A52 .	27
Scheme 1.2	Schematic illustration showing the reduction-triggered self-assembly of cyclic peptide A53 .	28
Scheme 1.3	Synthesis of <i>S</i> -benzyl-protected cysteine- and Phe-containing tripeptide A79 . Reagents and condition a) EDC·HCl, HOBt, TEA, 0 °C to r.t., 8 h; b) 4 M HCl in 1,4-dioxane, 0 °C to r.t., 2 h and c) Boc-Phe, EDC·HCl, HOBt, TEA, 0 °C to r.t., 8 h.	37
Scheme 1.4	Photo-induced conversion of hydrogel forming A118 to gel disrupting A119 .	54
Scheme 1.5	Subtilisin-catalyzed methyl ester hydrolysis of A142 .	67
Scheme 2.1	Synthesis of Boc-protected dipeptides and corresponding <i>N</i> -deprotected derivatives.	103
Scheme 3.1	Synthesis of anion receptors C1-C3 containing Leu, Phe and Trp, respectively.	157
Scheme 4.1	Synthetic route of diacetylene monomers D3 and D4 .	219
Scheme 4.2	Synthesis of Phe-appended polydiacetylenes PD3 and PD4 .	219
Scheme 5.1	Synthesis of lipidated Leu- and Glu-appended <i>exo</i> -norbornene-cored monomers E5-E10 .	255
Scheme 5.2	ROMP of monomers in the presence of Grubbs second generation catalyst to give polymers PE5-PE10 .	256
Scheme 5.3	Synthesis of <i>exo</i> -norbornene-cored monomers E13-E15 with aromatic appendages.	279
Scheme 5.4	ROMP of monomers in the presence of Grubbs second generation catalyst to give polymers PE13-PE15 .	280
Scheme 5.5	Synthesis of <i>endo</i> -norbornene-cored monomer E16 .	285

LIST OF ABBREVIATIONS

%	Percent
δ	Chemical shift
$^{\circ}\text{C}$	Degree centigrade
μ	Mobility
v_d	Drift velocity
λ	Wavelength
Φ	Barrier height
κ	Curvature
ΔF	Dehydrophenylalanine
μM	Micro molar
μm	Micro meter
μL	Micro litre
5-Fu	5-fluorouracil
ACN	Acetonitrile
ADP	Adenosine diphosphate
AFM	Atomic force microscopy
AIE	Aggregation-induced emission
Amoc	Anthracenemethoxycarbonyl
AMP	Adenosine monophosphate
aq.	Aqueous
Ar	Aryl
ArH	Aromatic proton
ATP	Adenosine triphosphate
ATR-IR	Attenuated total reflectance infrared
Boc	<i>tert</i> -butyloxycarbonyl
br	Broad
C	Oxide capacitance
CA	Chronoamperometry
CAC	Critical aggregation concentration

CD	Circular dichroism
CHCl ₃	Chloroform
CLSM	Confocal laser scanning microscopy
Conc.	Concentrated
CPT	Camptothecin
CuCl	Copper(I) Chloride
CV	Cyclic voltammetry
d	Doublet
Da	Dalton
DAPI	4',6-diamidino-2-phenylindole
DCC	N,N'-dicyclohexylcarbodiimide
DCM	Dichloromethane
dd	Double doublet
DFT	Density functional theory
DIC	Differential interference contrast
DIPEA	N,N'-Diisopropylethylamine
DLS	Dynamic light scattering
DMEM	Dulbecco's modified Eagle's medium
DMF	N,N-dimethylformamide
DMSO	Dimethylsulfoxide
DNP	Double numerical plus polarization
DOPA	3,4-dihydroxy-L-phenylalanine
DOX	Doxorubicin
DPBS	Dulbecco's phosphate buffered saline
DPV	Differential pulse voltammetry
DTNB	5,5'-dithio-bis(2-nitrobenzoic acid)
DTT	1,4 Dithiothreitol
E	Peak potential
E _A	Activation energy
ECM	Extracellular matrix
EDC·HCl	<i>N</i> -(3-dimethylaminopropyl)- <i>N</i> '-ethylcarbodiimide hydrochloride

EDOT-OH	Hydroxymethyl-(3,4-ethylenedioxythiophene)
EE	Encapsulation efficiency
E_{rel}	Relative energy
ESI	Electrospray ionization
EtOAc	Ethyl acetate
FBS	Fetal bovine serum
FET	Field effect transistor
FIB	Focused ion beam
Fmoc	9-fluorenylmethoxycarbonyl
FTIR	Fourier-transform infrared
g	Gram
G2	Grubbs second generation catalyst
GCE	Glassy carbon electrode
GGA	Generalized gradient approximation
GPC	Gel permeation chromatography
GSH	Glutathione
GTP	Guanosine triphosphate
h	Hour
HBS	Hank's buffered saline
HOMO	Highest occupied molecular orbital
HRMS	High resolution mass spectrometry
HRTEM	High resolution transmission electron microscope
Hz	Hertz
I	Peak current
I_{DS}	Drain to source current
IR	Infrared
ITC	Isothermal calorimetry
J	Coupling constant
k	Boltzmann constant
L	Channel length
LC	Loading capacity

LC-MS	Liquid chromatography-mass spectrometry
LED	Light emitting diode
LOD	Limit of detection
LOQ	Limit of quantification
LUMO	Lowest unoccupied molecular orbital
m	Multiplet
MD	Molecular dynamics
MeOH	Methanol
mg	Milli gram
min	Minutes
mL	Milli litre
mmol	Milli moles
MMP	Matrix metalloproteinase
mol	Mole
MP	Melting point
MTT	3-(4,5- dimethyl-2-thiazolyl)-2,5-diphenyltetrazolium bromide
MWCO	Molecular weight cut-off
m/z	Mass/charge
NCCS	National Centre for Cell Science
NDI	1,4,5,8-naphthalenetetracarboxylic diimide
NHE	Normal hydrogen electrode
NHS	<i>N</i> -hydroxysuccinimide
NMR	Nuclear magnetic resonance
NPT	Isothermal isobaric
NR	Nile red
OFET	Organic field effect transistor
PAG	Photoacid generator
PARP	Poly(ADP-ribose) polymerase
PB	Polybutadiene
PBS	Phosphate buffered saline
PDA	Polydiacetylene

PDF	Pair distribution function
PDI	Polydispersity Index
PEG	Polyethylene glycol
PGA	Poly(L-glutamic acid)
ppm	Parts per million
PXRD	Powder X-ray diffraction
Py	Pyrene
q	Quartet
QC	Quantum confinement
QCM-D	Quartz crystal microbalance
RAFT	Regioselectively addressable functional template
RB	Rhodamine B
ROMP	Ring opening metathesis polymerization
RT	Room temperature
s	Singlet
SAM	Self-assembled monolayer
SANS	Small-angle neutron scattering
SAXS	Small-angle x-ray scattering
SCE	Saturated calomel electrode
SD	Standard deviation
SEM	Scanning electron microscopy
SS	Subthreshold slope
t	Triplet
T	Temperature
TBA	Tetrabutylammonium
TBABF ₄	Tetrabutylammonium tetrafluoroborate
TBAF	Tetrabutylammonium fluoride
TBAH ₂ PO ₄	Tetrabutylammonium dihydrogen phosphate
TBAP	Tetrabutylammonium perchlorate
TEA	Triethylamine
TEG	Tri(ethylene glycol)

TFA	Trifluoroacetic acid
THF	Tetrahydrofuran
TLC	Thin layer chromatography
TMEDA	Tetramethylethylenediamine
TMS	Tetramethylsilane
TPE	Tetraphenylethylene
TTF	Tetrathiafulvalene
UV	Ultraviolet
V_{DS}	Drain to source voltage
V_{GS}	Gate to source voltage
Vis	Visible
W	Channel width
WAXS	Wide-angle X-ray scattering
WCA	Water contact angle

NOTES

1. All amino acids used in syntheses were of L-configuration and were purchased from SRL India. Unless, otherwise stated, the standard single/triple letter codes are used to represent amino acids.
2. All commercial chemicals and reagents used in chemical syntheses were purchased from Sigma-Aldrich or Alfa Aesar unless, otherwise stated and used as received without any further purification.
3. All the solvents employed in the reactions were distilled/dried by standard protocols prior to use.
4. All air sensitive reactions were carried out in oven dried glassware under an inert atmosphere of argon.
5. All the reactions were monitored by silica gel thin layer chromatography (TLC), wherever possible.
6. All the synthesized compounds were purified by silica gel (100-200 mesh) column chromatography. The slurry was generally made in chloroform, DCM and/or MeOH.
7. The characterization of synthesized compounds was done by ^1H NMR, ^{13}C NMR, IR and High Resolution Mass Spectrometry (HRMS).
8. ^1H and ^{13}C NMR spectra were recorded on a Bruker-DPX-300/400/500 MHz spectrometer and the chemical shifts are reported downfield relative to tetramethylsilane (TMS). ^1H NMR data are reported as br (broad), s (singlet), d (doublet), q (quartet), t (triplet) and m (multiplet). ^1H NMR coupling constants are reported in Hz.
9. High resolution mass spectra (HRMS) were recorded in Bruker Micro-TOF-QII model using Electrospray Ionization (ESI) technique.

10. IR spectra were recorded on Agilent-Cary 660 Series FTIR spectrometer/Nicolet, Protégé 460 spectrometer as KBr Pellets.
11. Attenuated Total Reflectance Infrared (ATR-IR) spectra were recorded on an Agilent-Cary 660 Series FTIR spectrometer. For ATR-IR, the samples were placed on the diamond sample holder and 32 scans were performed on each sample.
12. Melting points were recorded on a Fisher-Scientific melting point apparatus.